Supplement of Hydrol. Earth Syst. Sci., 29, 6685–6702, 2025
https://doi.org/10.5194/hess-29-6685-2025-supplement

Hydrology and Earth System Sciences
Open Access
EGU

Supplement of

Evolution of low-karstified rock-blocks and their influence on reservoir leakage: a modelling perspective

Youjun Jiao et al.

Correspondence to: Franci Gabrovšek (franci.gabrovsek@zrc-sazu.si) and Qingchun Yu (yuqch@cugb.edu.cn)

S1 Model details & validation

The flowchart of the flow solution is shown in Figure S1. At each time step, the convergence status is recorded in the runtime output file. An example is available on our GitHub repository at Fracturetokarst2024/slurm-17392021.out. This file includes key indicators such as the number of iterations required for solving the iterative flow equations for confined flow solver, water head errors, and total flux balance. Iterations are controlled internally both node-by-node and layer-by-layer. If the confined flow solver encounters convergence issues, the model reverts to the last successful state and proceeds by testing the next dry node. To assess the model's accuracy, results were benchmarked against MODFLOW simulations, as described in the subsequent section.

We also explored the model's behaviour under different flow regimes by simulating the coexistence of turbulent and laminar flows. These tests confirmed the numerical stability of the model. Additionally, the model is capable of generating random fractures, which are used directly in flow and dissolution computations. These fractures vary in shape and size and are not constrained by the underlying computational grid.

A high-performance computing environment is essential for achieving long-term stability in water table simulations. The calculations were performed on a platform using a Chinese Hygon C86 7185 32-core processor, running CentOS Linux 7. For these simulations, we utilized 8 cores on a single compute node.

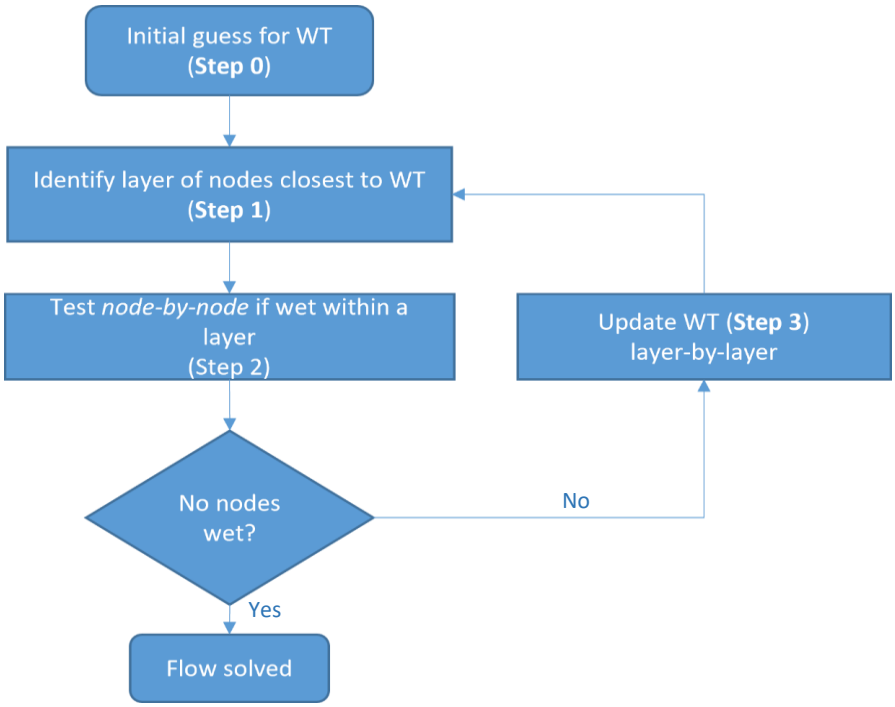

Figure S1. Flowchart of the flow solution.

S 2 Test of the water table in a homogeneous fractured aquifer

To verify the numerical model, we first compare the results for the homogeneous network with MODFLOW (Harbaugh et al., 2000) and the analytical solution derived using the Dupuit assumption, which can be expressed as follows:

$$H=\sqrt{H_0^2-\frac{w}{K_x}X^2+\frac{w\,S}{K_x}X} \tag{S1}$$

Where H_0 is the river base level, K_x is the equivalent horizontal conductivity in m/d, S is the aquifer length, X is the distance from the left river boundary, and w is the intensity of rainfall recharge.

The homogeneous fracture network is shown in Figure S2. We assume translational symmetry and therefore use 2D domain populated by fracture. The horizontal dimension of the domain is 1000 m and vertical 400 m. The distance between the fractures in both the X direction and the Y direction is 10 m. The aperture is 0.01 cm for all the fractures. Along the two

side boundaries, nodes lower than 200 m in height are given a constant water head of 200 m. Nodes above 200 m have seepage boundary conditions. The two recharge conditions were tested at 400 mm/a and 800 mm/a.

Within the MODFLOW validation, we calculate the equivalent horizontal K_x and vertical K_y by treating the aquifer as having confined water head boundaries in the X and Y directions, respectively. The conductivities are proportional to the ratio between the resulting flux and the head difference. The horizontal and vertical K values are virtually identical, both approximately 0.00705 m/d. The DRAIN module in MODFLOW was used to model the seepage face by setting each boundary node above the constant head with drainage function, which worked as its water head became higher than the drain's elevation. In Figure S2, water table nodes are labelled blue and the corresponding heads have orange labels. The water tables obtained via the Dupuit assumption are always lower than the simulated water table since the vertical flow and seepage face are not considered. Note that the heads at water table nodes are higher than their elevation, but below the elevation of the nearest dry node above them. The water tables simulated with our method are nearly the same as the MODFLOW simulation. Additionally, we can see the seepage face boundaries on both sides, which evidently do not exist in the analytical solution.

We have taken additional steps to evaluate the performance of our model. Specifically, we varied grid sizes and recharge rates and calculated the root mean square difference (RMS) in water heads at water table nodes between our solution and that obtained with MODFLOW. The results are summarized in Table S1. Three grid sizes and three recharge rates were tested while keeping the aperture fixed. To ensure comparability between models, we used an equivalent hydraulic conductivity in MODFLOW and the corresponding discretization. The RMS of water heads is approximately one quarter of the grid size and increases with recharge rate as shown in Table S1. The analysis demonstrates the effectiveness of our algorithm.

$$RMS = \sqrt{\frac{1}{n}\sum_{i=1}^{n}(y_i - \hat{y}_i)^2} \tag{S2}$$

Where y_i is the MODFLOW water head, and $\hat{y}_i$ is our method's water head at a water table node, and n is the number of water heads.

Table S1 The model fit between our method and the MODFLOW solution with different grid sizes and recharge rates

aperture(cm)	grid size (m)	equivalent hydraulic conductivity K (m/d)	recharge rate (mm/a)	layer-by-layer iterations	RMS difference of water heads at water table nodes (m)
0.01	10	0.00705	200	19	1.27
0.01	10	0.00705	400	23	2.45
0.01	10	0.00705	800	34	2.77
0.01	15	0.00473	400	20	2.11
0.01	20	0.00353	400	19	5.07

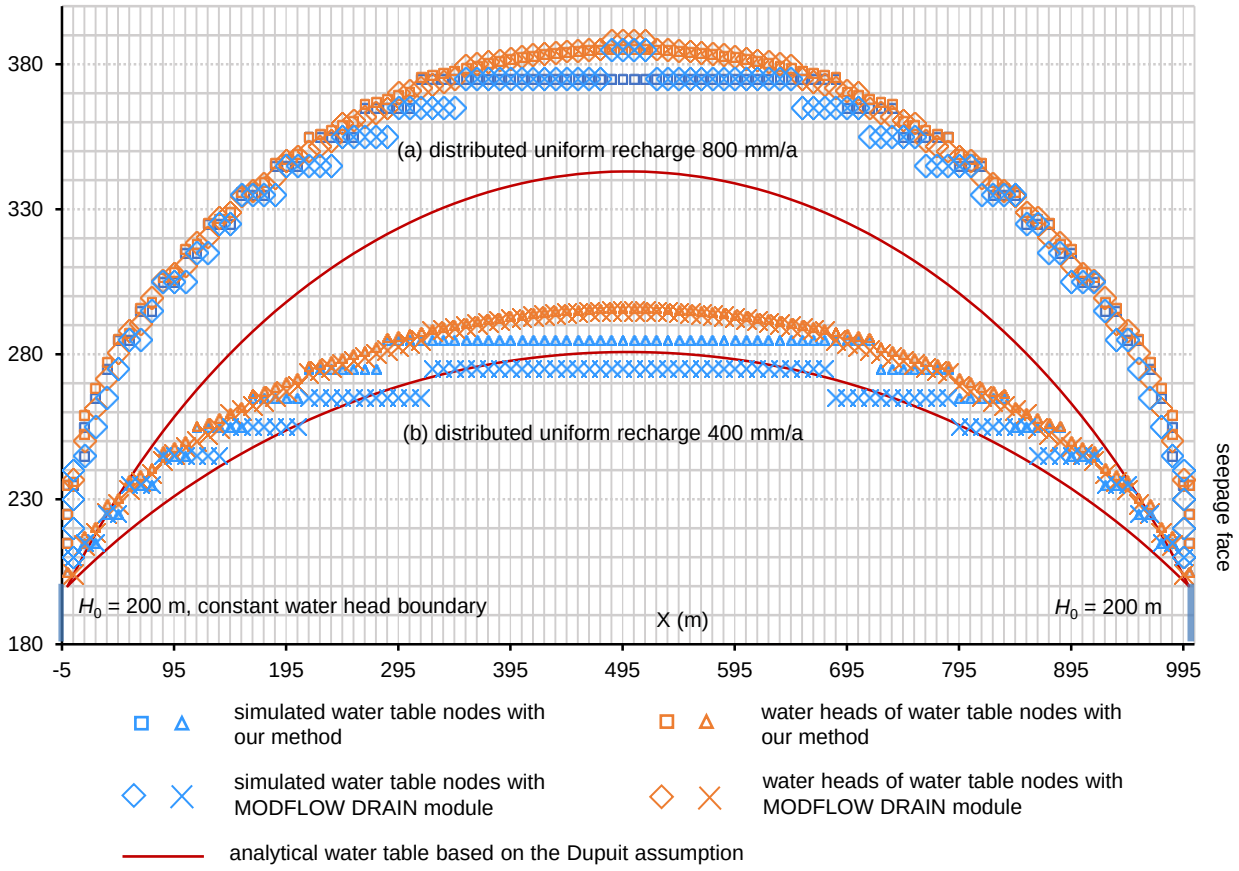

Figure S2. Water tables and corresponding heads validation with MODFLOW and Dupuit analytical models for two distributed uniform recharge conditions.

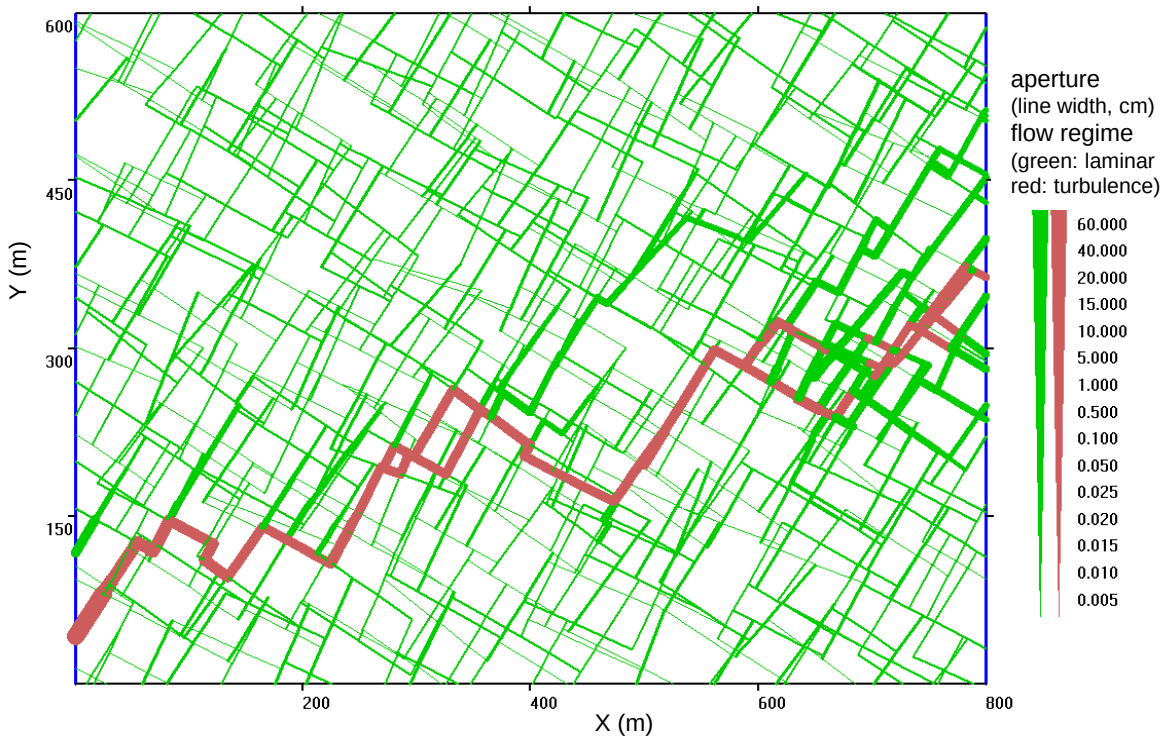

Figure S3. The iterative solution of turbulent and laminar flow (Jiao et. al, 2022).

Although it is not relevant for the results presented in this work, as shown in Figure S3,we explored the inner iteration of confined flow under different flow regimes by simulating the coexistence of turbulent and laminar flows (Jiao et. al, 2022). For a typical case of about 3000 fractures, the number of iterations in Newton-Raphson scheme is about 2, when laminar regime is present in the entire domain. At the onset of turbulence the number of iterations jumps to 15. During turbulent regime the number of iterations is kept low (below 10) by keeping the evolution time step small enough, i.e. we ensure small change of hydraulic properties within time-step.

S3 Modelling a water table in a heterogeneous fractured aquifer

The next step is to test the solution for heterogeneous network. We use the same setting as for the homogenous network but with random generation of fractures and two recharge conditions, 200 mm/a and 400 mm/a. The equivalent horizontal and vertical K values are 0.00469 m/d and 0.00434 m/d, respectively. The number of outer iterations in all evolving time steps varied from 5 to 35. The process of searching for a water table takes approximately 3 to 4 hours during

the initial modelling stages of karst evolution, and it is performed on a high-performance computing platform that utilizes 8 cores.

The fracture flow and water table data are shown in Figure S4 and Figure S5. The water table is discontinuous because of the inhomogeneous distribution of fractures. Only a few nodes for the simulated water table are lower than the analytical water table. The difference between the elevation and head at water table nodes varies due to the heterogeneity of the network. The seepage faces above the constant head boundaries on the both sides of the domain, are successfully simulated as the Signorini boundary (Jiang et al., 2013). Considering these two recharge conditions, the algorithm performed well in modelling the water table in heterogeneous network.

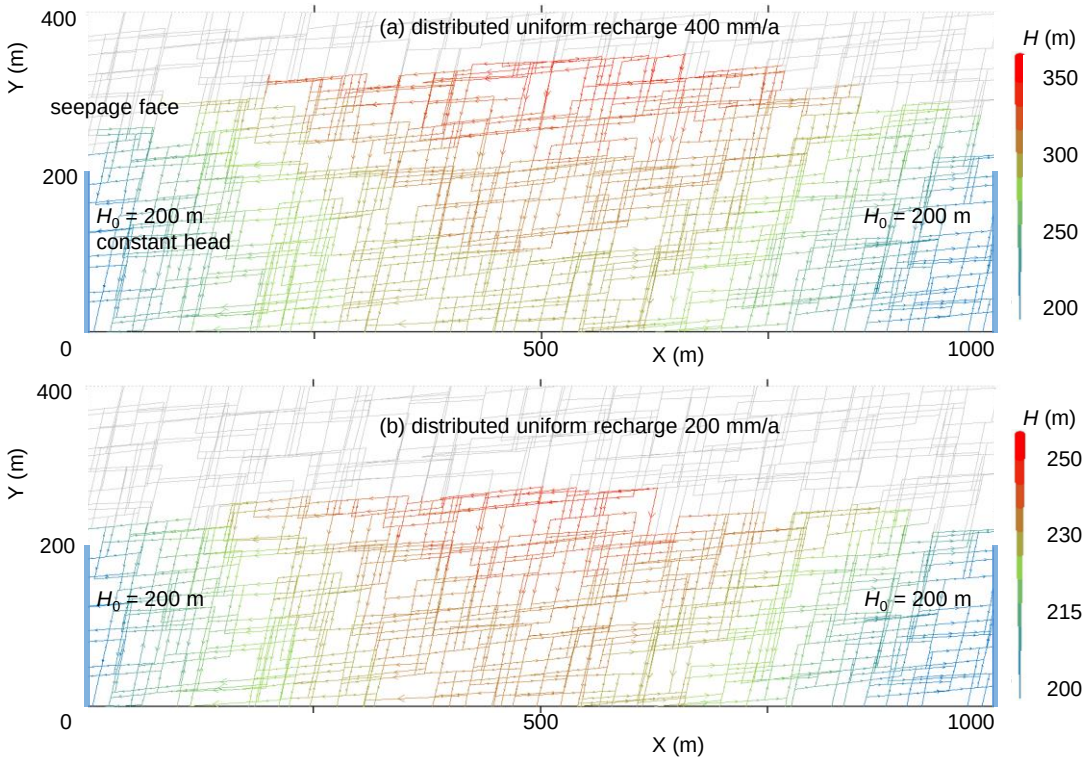

Figure S4. Modelling the phreatic flow in random fractures under 400mm/a and 200mm/a distributed uniform recharge conditions.

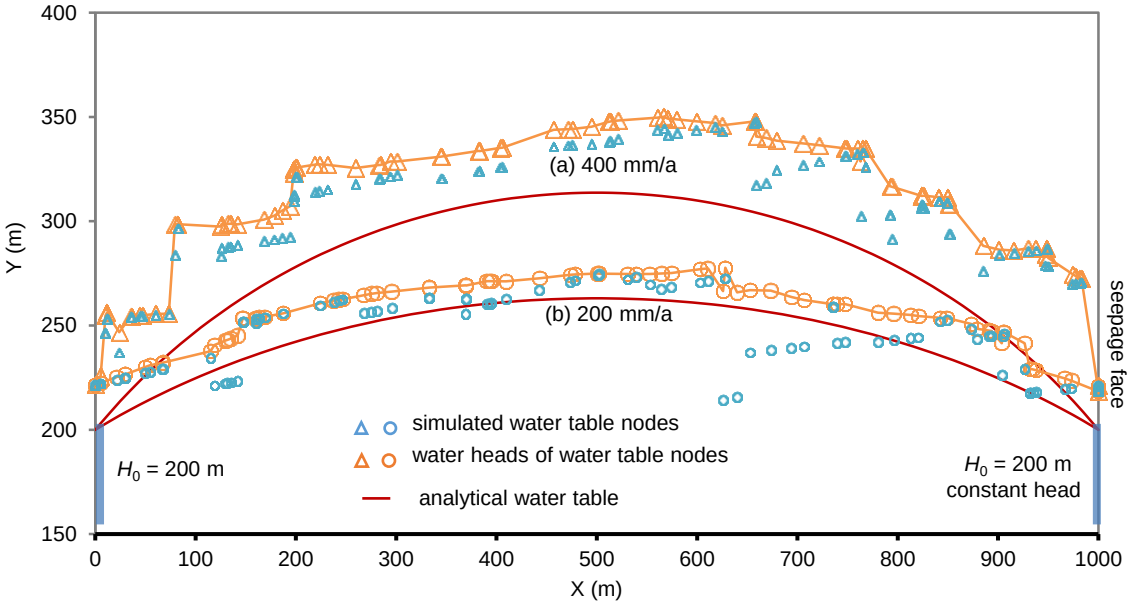

Figure S5. The simulated and analytical results of random fracture water tables and water heads of corresponding nodes.

S4 Calculating dissolution and transport on a fracture and network scale

S4.1 Dissolution and change of concentration along an individual fracture

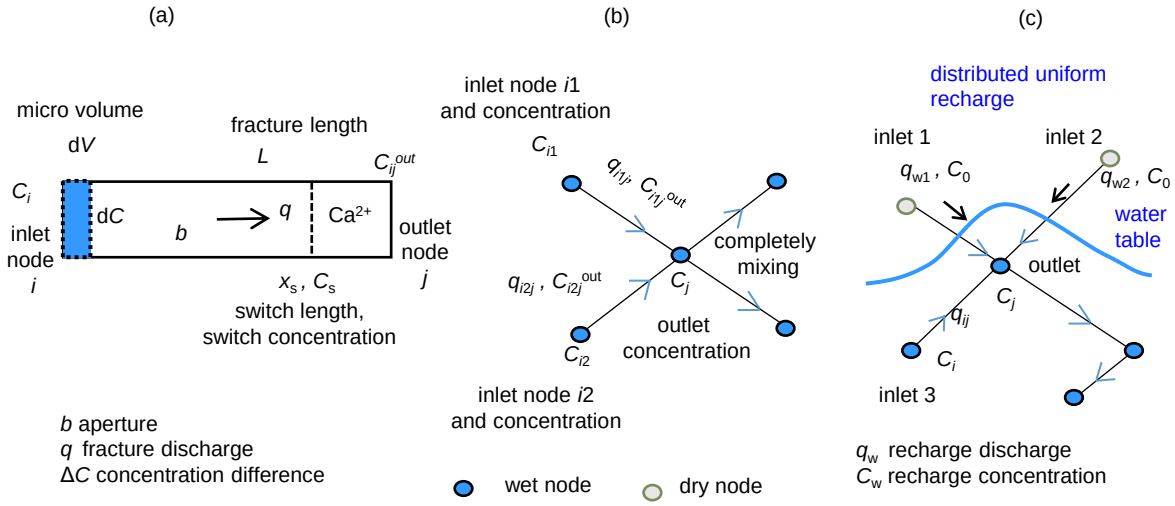

Figure S6. Calculating Ca^{2+} concentration along one single fracture and at fractures joint node and near the water table.

To calculate change of concentration within a single fracture, we use a Lagrangian approach and imagine a water parcel with volume $dV=Pdx$ moving along the fracture with velocity $v=Q/A$, where A is a flow crosssection, and calculate the change of concentration within the parcel (Figure S6a). In a time dt the change of concentration in a parcel is equal to:

$$dC = F(c) \cdot P \cdot dx \cdot \ dt/dV \tag{S3}$$

Where P is flow perimeter and Pdx is the surface area of water/rock contact. Rearranging the equation gives:

$$\int_{C_i}^{c(x)} \frac{dc}{F(c)} = \frac{P}{Q}x = \frac{2(b+w)}{qw}x \approx \frac{2}{q}x \tag{S4}$$

The last term is an approximation for a wide fracture with the lateral width w and aperture b, where $w>>b$; q is flow rate per unit width. Using rate Equations (Eq. 7 and Eq. 8) for $F(c)$, we get:

$$C(x) = C_{\mathrm{eq}} - \left(C_{\mathrm{eq}} - C_i\right)e^{-\left(\frac{2k_1}{q\,C_{\mathrm{eq}}}x\right)}, \quad (C < C_s) \tag{S5}$$

$$C(x) = C_{\mathrm{eq}} - C_{\mathrm{eq}}\left(C_{\mathrm{eq}} - C_i\right)\sqrt[3]{\frac{q\,C_{\mathrm{eq}}}{\left(C_{\mathrm{eq}} - C_i\right)^3 6k_4 x + q\,C_{\mathrm{eq}}{}^4}}, \left(C_s < C < C_{\mathrm{eq}}\right) \tag{S6}$$

Where k_1 and k_4 are rate constants. C_{eq} and C_{s} are the equilibrium concentration and the switch concentration of Ca^{2+} ions.

The change of concentration ΔC at the outlet of the fracture is given by:

$$\Delta C = C_{eq} - C_{eq}e^{-\left(\frac{2k_1}{q\,C_{eq}}L\right)} + C_i\left(e^{-\left(\frac{2k_1}{q\,C_{eq}}L\right)} - 1\right), \ (\ C_i < C_s, x_s > L) \tag{S7}$$

$$\Delta C = C_{eq} - C_i - 0.1\,C_{eq}^2\sqrt[3]{\frac{q\,C_{eq}}{\left(0.1C_{eq}\right)^3 6k_4 L + q\,C_{eq}{}^4}}, (C_i < C_s, x_s < L) \tag{S8}$$

$$\Delta C = C_{eq} - C_i - C_{eq}^2\sqrt[3]{\frac{q\,C_{eq}}{\left(C_{eq} - C_i\right)^3 6k_4 L + q\,C_{eq}{}^4}} + C_{eq}C_i\sqrt[3]{\frac{q\,C_{eq}}{\left(C_{eq} - C_i\right)^3 6k_4 L + q\,C_{eq}{}^4}}, \ (\ C_i > C_s) \tag{S9}$$

Where x_{s} is the switch distance of C_{s}. If $C_i < C_{\mathrm{s}}$ and $x_{\mathrm{s}} > L$, dissolved mass is calculated from Eq. S7. If $C_i < C_{\mathrm{s}}$ and $x_{\mathrm{s}} < L$, Eq. S8 is used. If $C_i > C_{\mathrm{s}}$, Eq. S9 is used for dissolved mass directly.

S4.2 Following concentration at the network scale

To assure that concentrations at the input nodes are always known, we follow the procedure of Siemers and Dreybrodt (1998) and Gabrovšek and Dreybrodt (2000). The process begins at the network's boundary nodes with the highest hydraulic heads, where head or flux values and concentrations are prescribed. Calculations then proceed sequentially along the hydraulic gradient. As illustrated in Figure S6b and c, the concentration C_j at the node j is calculated using the complete mixing assumption. This involves computing the flow-weighted average of the incoming concentrations:

$$c_j = \frac{\sum_i c_{ij}^{out} q_{ij} + \sum_k C_0 q_{wk}}{\sum_i q_{ij} + \sum_k q_{wk}} \tag{S10}$$

Where q_{wk} and C_0 are flow and concentration of direct recharge at water table nodes; q_{ij} and C_{ij}^{out} are the output flow and concentration of fractures connecting nodes i and j; i sums over confined nodes that deliver flow to j, and k runs over direct input at the water table.

S5 Random realizations of kastification of fracture network in the field site

Characterizing a fracture network for a specific field site remains a significant challenge. In this study, we employed field-relevant fracture orientations, while the initial aperture and length distributions were assigned heuristically, consistent with approaches used by other researchers. The configuration of the initial fracture network strongly influences the evolution of the aquifer. To assess this sensitivity, we tested several realizations (Figure S7) and obtained conceptually identical results.

Chemical analyses of the borehole samples indicate that the water is nearly saturated with respect to calcite (Yuan et al., 2002; Wan et al., 1999), as shown in Figure S8. Numerous studies have reported high saturation levels of infiltrating water within the vadose zone (e.g., Fairchild and Baker, 2012). Furthermore, during the initial stages of karst aquifer development, equilibrium with calcite is typically achieved over very short distances (Dreybrodt et al., 2005). Thus, even when the initial calcium concentration is low, saturation conditions—under which such an approximation remains valid—are usually reached within a few meters.

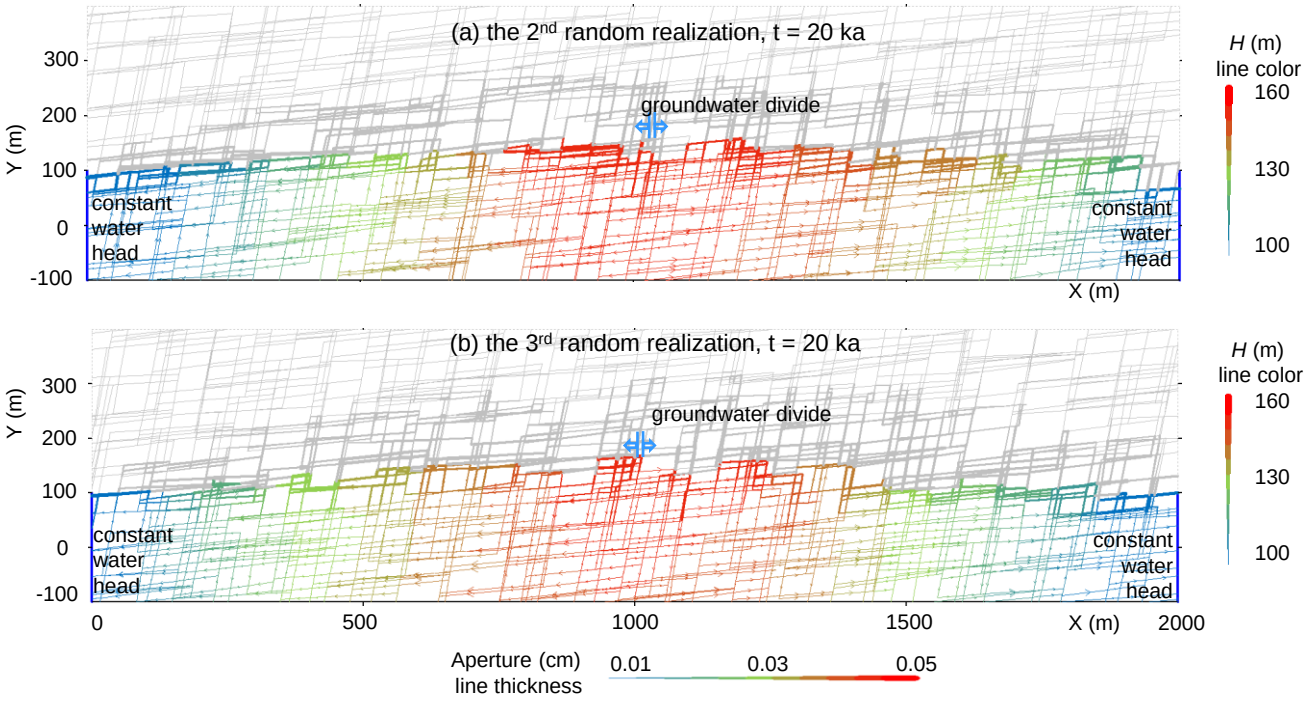

Figure S7. The other two random realizations of karstification in the interfluve aquifer

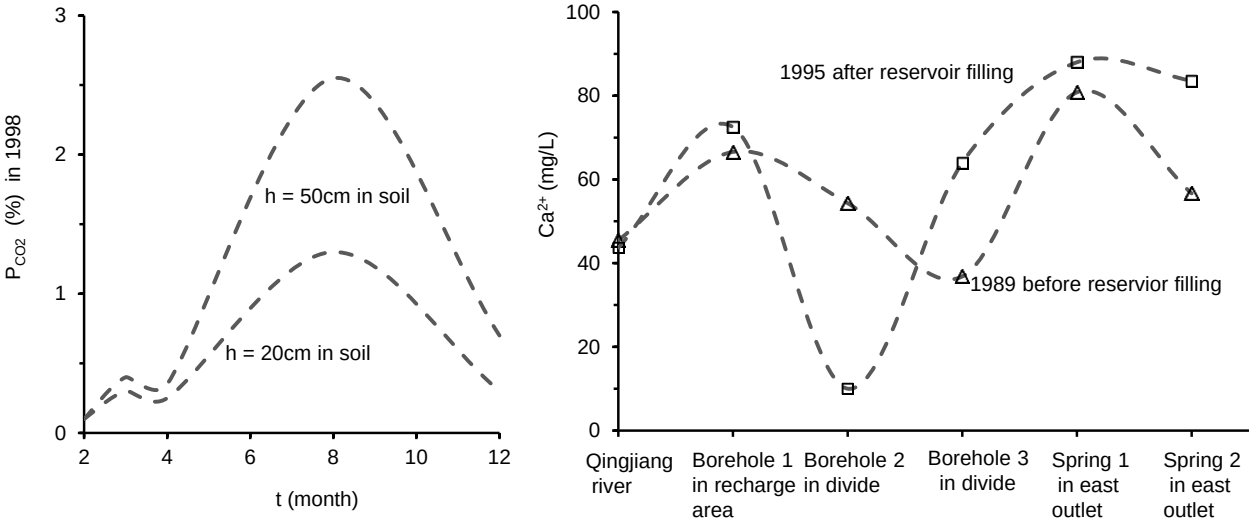

Figure S8. The CO2 partial pressure in the soil at the Luojiaao observation site and the Ca2+ content in 3 boreholes and 2 springs in the Luojiaao interfluve aquifer (Yuan et al., 2002; Wan et al., 1999)

References

Fairchild, I. J., and Baker, A.: Speleothem science: from process to past environments, John Wiley & Sons, 2012.

Gabrovšek, F., and Dreybrodt, W.: Role of mixing corrosion in calcite-aggressive H_2O-CO_2-$CaCO_3$ solutions in the early evolution of karst aquifers in limestone, Water Resour. Res., 36, 1179-1188, https://doi.org/10.1029/1999WR900337, 2000.

Harbaugh, A. W., Banta, E. R., Hill, M. C., and McDonald, M. G.: MODFLOW-2000, the US Geological Survey modular ground-water model: User guide to modularization concepts and the ground-water flow process, U.S. GEOLOGICAL SURVEY, Open-File Report 00-92, https://doi.org/10.3133/ofr200092, 2000.

Jiang, Q., Yao, C., Ye, Z., and Zhou, C.: Seepage flow with free surface in fracture networks, Water Resour. Res., 49, 176-186, https://doi.org/10.1029/2012WR011991, 2013.

Jiao, Y., Huang, Q., and Yu, Q.: Influence of initial fractures on the occurrence of karst turbulent flow, Carsologica Sinica, 41, 501-510, (in Chinese), https://doi.org/10.11932/karst20220401, 2022.

Siemers, J., and Dreybrodt, W.: Early development of karst aquifers on percolation networks of fractures in limestone, Water Resour. Res., 34, 409-419, https://doi.org/10.1029/97WR03218, 1998.

Wan, J., Chao, N., Shen, J., and Cai, J.: Study on the carbon cycle in a karst system at the Luojiaao interfluve along the Qingjiang River of western Hubei, China, Carsologica Sinica, 18, 123-128, (in Chinese), https://doi.org/10.3969/j.issn.1001-4810.1999.02.004, 1999.

Yuan, D., Liu, Z., Lin, Y., Shen, J., He, S., Xu, S., Yang, L., Li, B., Qin, J., Cai, W., Cao, J., Zhang, M., Jiang, Z., and Zhao, J.: Karst dynamic system of China, Geological Publishing House, Beijing, (in Chinese), 2002.